Isochronous mass measurements of neutron-deficient nuclei from ^{112}Sn projectile fragmentation

Y. M. Xing,[1] C. X. Yuan,[2] M. Wang,[1,*] Y. H. Zhang,[1,†] X. H. Zhou,[1] Yu. A. Litvinov,[1,3] K. Blaum,[4] H. S. Xu,[1] T. Bao,[1] R. J. Chen,[1,3] C. Y. Fu,[1] B. S. Gao,[1] W. W. Ge,[1] J. J. He,[5,6] W. J. Huang,[7,1] T. Liao,[1,8] J. G. Li,[1] H. F. Li,[1,8] S. Litvinov,[3] S. Naimi,[9] P. Shuai,[1] M. Z. Sun,[1] Q. Wang,[1,8] X. Xu,[1] F. R. Xu,[10] T. Yamaguchi,[11] X. L. Yan,[1] J. C. Yang,[1] Y. J. Yuan,[1] Q. Zeng,[12,1] M. Zhang,[1,8] and X. Zhou[1,8]

[1]*Key Laboratory of High Precision Nuclear Spectroscopy and Center for Nuclear Matter Science, Institute of Modern Physics, Chinese Academy of Sciences, Lanzhou 730000, People's Republic of China*

[2]*Sino-French Institute of Nuclear Engineering and Technology, Sun Yat-Sen University, Zhuhai 519082, China*

[3]*GSI Helmholtz Centre for Heavy Ion Research, Darmstadt 64291, Germany*

[4]*Max-Planck-Institut für Kernphysik, Heidelberg 69117, Germany*

[5]*Key Laboratory of Beam Technology of Ministry of Education, College of Nuclear Science and Technology, Beijing Normal University, Beijing 100875, China*

[6]*Institute of Radiation Technology, Beijing Academy of Science and Technology, Beijing 100875, China*

[7]*Advanced Energy Science and Technology Guangdong Laboratory, Huizhou 516007, China*

[8]*University of Chinese Academy of Sciences, Beijing 100049, People's Republic of China*

[9]*RIKEN Nishina Center, RIKEN, Saitama 351-0198, Japan*

[10]*State Key Laboratory of Nuclear Physics and Technology, School of Physics, Peking University, Beijing 100871, People's Republic of China*

[11]*Department of Physics, Saitama University, Saitama 338-8570, Japan*

[12]*School of Nuclear Science and Engineering, East China University of Technology, Nanchang 330013, China*

(Received 30 March 2022; accepted 9 December 2022; published 11 January 2023)

Masses of ^{112}Sn projectile fragments were measured employing isochronous mass spectrometry at the Cooler Storage Ring in Lanzhou. Different from the previous data analysis method, relying on the arithmetic mean revolution times of the stored fragments, we introduce an exponentially modified Gaussian function to describe the asymmetric peak shapes. This new approach enables us to properly deconvolute the overlapping peaks of stored ions and to accurately determine their masses. The mass excesses of ^{103}Sn and the low-lying $1/2^-$ isomers in ^{87}Mo, ^{91}Ru, and ^{95}Pd were directly measured for the first time, and the masses of ^{69}As, ^{73}Br, ^{75}Kr, ^{79}Sr, and ^{81}Y were redetermined with higher precision comparable to that of Penning-trap mass spectrometry. Based on the new mass value of ^{103}Sn, the previously unknown masses of ^{104}Sb, ^{107}Te, ^{108}I, ^{111}Xe, and ^{112}Cs were obtained indirectly by using the literature proton and/or α decay energies. Systematic trends of the excitation energies of the $J^\pi = 1/2^-$ isomers in the $N = 47,\ 49$ isotones are well reproduced by the state-of-the-art shell model calculations with the tensor forces included.

DOI: 10.1103/PhysRevC.107.014304

I. INTRODUCTION

The mass of an atomic nucleus is a fundamental quantity reflecting all the interactions acting among constituent nucleons. Nuclear masses are extensively used to study nuclear properties including, but not limited to, nuclear forces, evolution of shapes, separation energies, reaction rates, and so on [1]. Furthermore, the masses of long-lived isomers are of high interest in nuclear structure [2,3] and nuclear astrophysics [4–8].

Tremendous efforts have been made to directly measure nuclear masses using different techniques, such as time-of-flight magnetic-rigidity (TOF-$B\rho$) mass measurement method [9], Penning-trap mass spectrometry (PTMS) [10], multireflection TOF mass spectrometry (MR-TOF-MS) [11], and storage-ring based isochronous mass spectrometry (IMS) [12] and Schottky mass spectrometry (SMS) [13]. As of today, the mass measurements are pushed to exotic nuclei with extremely low production yields and short half-lives. In this context, isochronous mass spectrometry (IMS), established in ESR/GSI [14], CSRe/IMP [15], and R3/RIKEN [16], has been proven to be a powerful tool for mass measurements of such very exotic nuclei. Using this technique, numerous high-precision mass data [16–22] have been provided in the last years.

Up to date, most of the precise mass measurements of neutron-deficient nuclei in the upper fp shell below $A = 100$ mainly rely on the Penning-trap results, giving important mass data for studies in nuclear structure and nuclear astrophysics [23–25]. However such Penning-trap mass measurements are restricted by the stopping, extraction, and excitation procedures [26], which limit the short-lived nuclei and isomers to be

*wangm@impcas.ac.cn
†yhzhang@impcas.ac.cn

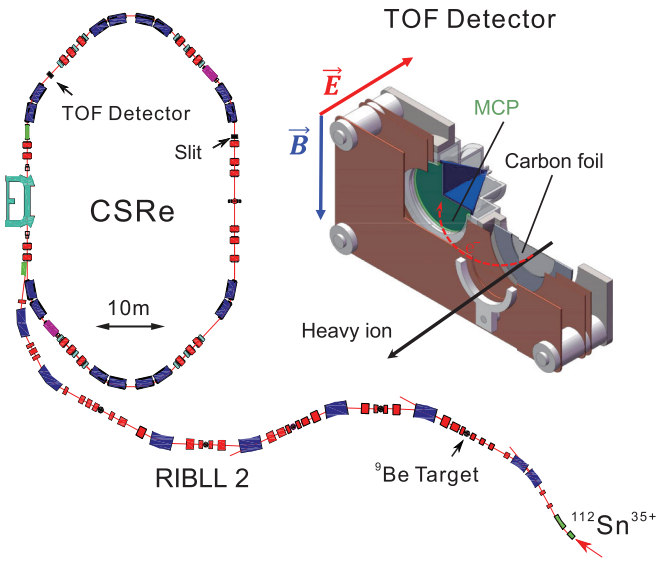

FIG. 1. Layout of RIBLL2 and CSRe machines at IMP, Lanzhou [34]. The locations of the TOF detector and the slit are indicated. The TOF detector is shown schematically in the insert [17]. Major components are labelled. For further details see text.

collected and measured. Recently, MR-TOF-MS has become available for mass measurements of the isomers in this region, and new mass data have been obtained using this technique [27,28].

An IMS mass measurement of ^{112}Sn projectile fragments was performed in CSRe/IMP, and some of neutron-deficient nuclei in the mass region of $A \simeq 70$–100 were observed to be in both ground and isomeric states. The mass value of a $1/2^-$ isomer in ^{101}In obtained from this experiment has shed light on the shell evolution due to tensor force [29]. Previous data analyses used the arithmetic mean revolution times to determine the nuclear masses of ion species [29,30]. However, the time peaks were found to be asymmetric. It is thus difficult to deconvolute accurately the overlapping peaks corresponding either to the same ion species in ground and isomeric states, or to different ions with nearly identical mass-to-charge ratios. In this work, a skewed nonGaussian function, i.e., the exponentially modified Gaussian (EMG) function [31,32], is adopted to analyze the revolution time peaks for mass determinations.

The experiment and new data analysis are described in Sec. II where the validation of the method is justified by the precise redetermination of mass values of reference nuclei. In Sec. III, new mass values are reported focusing on the masses of the low-lying isomers. The energy systematics of the $J^\pi = 1/2^-$ isomers is also investigated in this section with help of state-of-the-art shell model calculations, and importance of the tensor force is emphasized. The conclusion and outlook are given in Sec. IV. Some results from this experiment have already been reported in Refs. [29,30].

II. EXPERIMENT AND DATA ANALYSIS

A. Measurement

The IMS experiment using the ^{112}Sn primary beam was performed at the HIRFL-CSR accelerator complex [33] at the Institute of Modern Physics (IMP) in Lanzhou, China. A layout of the second Radioactive Ion Beam Line at Lanzhou (RIBLL2) and the experimental Cooler Storage Ring (CSRe) is presented in Fig. 1. Experimental settings are listed in Table I.

TABLE I. The settings of the experiment.

Primary beam	^{112}Sn^{35+}
Energy	400.88 MeV/u
Intensity	8×10^7 particles per spill
$B\rho$ (Magnetic rigidity)	5.3347 Tm
$\Delta B/B$[a]	5.5×10^{-4}
Slit[b]	Yes
$\Delta p/p$ (FWHM)[c]	9×10^{-4}
γ_t of CSRe	1.302

[a]The instability of magnetic field during the experiment [35].
[b]A 50-mm-wide slit in the dispersive plane of CSRe was used to reduce the momentum acceptance.
[c]The estimated momentum acceptance [35].

Primary beam of ^{112}Sn^{35+} ions was accumulated and accelerated to a relativistic energy of about 400.88 MeV/u by the main Cooler Storage Ring (CSRm). Every 25 s, the beam was fast-extracted and focused onto a 10 mm thick beryllium target at the entrance of RIBLL2. Neutron-deficient nuclei of interest were produced via projectile fragmentation of ^{112}Sn^{35+}. The majority of fragments emerged from the target were fully ionized bare nuclei. They were separated in flight with RIBLL2 and injected into CSRe, which has a circumference of 128.8 m. CSRe was tuned into the isochronous ion-optical mode with the transition energy of $\gamma_t = 1.302$. The magnetic rigidity of the RIBLL2 and CSRe were determined to make the $T_z = 3/2$ ^{101}In^{49+} ions fulfill the isochronous condition of $\gamma = \gamma_t$, where γ is the relativistic Lorenz factor. The required energy of the primary beam was determined with LISE++ simulation [36] and optimized in the experiment to achieve the maximum yield of ^{101}In^{49+} ions. To improve the mass resolving power, a 50-mm-wide slit was installed in the dispersive plane [37] to reduce the $B\rho$ acceptance. The resultant $B\rho$ (momentum) acceptance was about 9×10^{-4} (FWHM).

To measure the revolution times of the stored ions, a TOF detector was utilized. It is equipped with a carbon foil (thickness ~19 μg/cm^2, diameter ~40 mm) and a set of multichannel plates (MCP) [38] (see Fig. 1). When an ion passed through the carbon foil, secondary electrons were released and guided isochronously to MCP by perpendicularly arranged electric ($\vec{E}$) and magnetic ($\vec{B}$) fields. The timing signals from the anode were directly fed without amplification into a fast digital oscilloscope with sampling rate of 40 GHz. The recording time was 200 μs for each injection of fresh ions into CSRe. Each revolving particle caused a train of timing signals recorded by the detector, which was then used to determine its revolution time, T. Revolution times of all stored ions were extracted according to the procedures described in detail in Refs. [39,40].

Instability of power supplies of the CSRe magnets led to magnetic field fluctuations on the order of $\Delta B/B \sim 10^{-4}$.

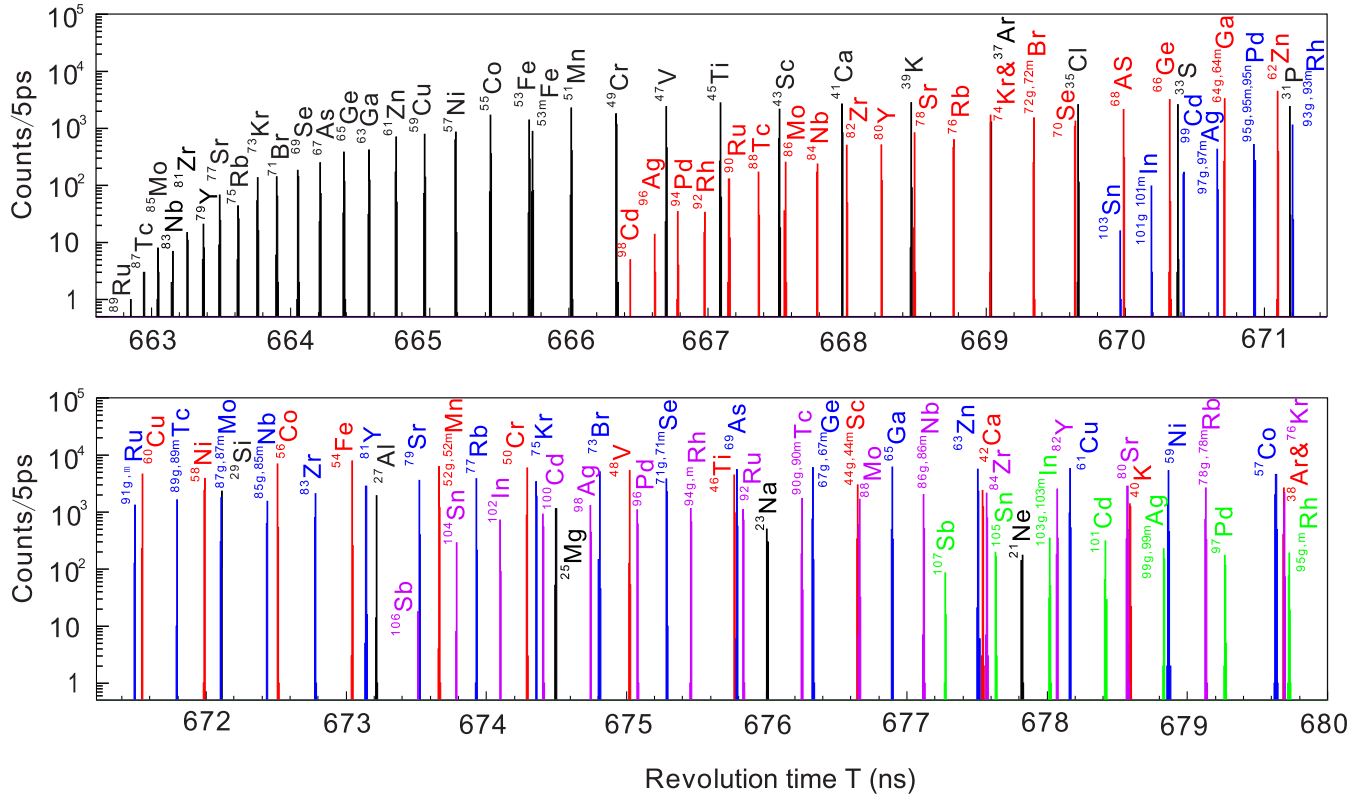

FIG. 2. Accumulated revolution time spectra after correction for magnetic field instability. The black, red, blue, violet, and green peaks represent the nuclei with $T_z = 1/2$, 1, 3/2, 2, and 5/2 respectively. The indices "g" and "m" or "n" represent the ground and isomeric state, respectively.

This instability resulted in a dramatic variation of T up to ∼100 ps [35], which was larger than the T difference of some neighboring peaks. This complicated the particle identification and seriously deteriorated the mass resolving power. To solve this problem, particle identification and T correction methods on an injection-by-injection basis had been developed [35].

In the present analysis, the method described in Ref. [35] was adopted. The T correction procedure for the reference ions with well known masses has been slightly modified: the T correction for a given reference ion was made by using data only from other reference ions in the same injection. In this way, all the ions, both references or nonreferences, were treated equally. This makes the standard deviations of the T distributions, σ_T, of reference and nonreference ions to be consistent with each other. The revolution time spectra after T correction procedure are shown in Fig. 2. The unambiguous particle identification was done in the same way as described in Ref. [35]. The nuclei noted in Fig. 2 are shown in the partial nuclidic chart in Fig. 3.

B. Peak shape analysis

In the previous IMS mass measurements, peak shapes of the T distributions were considered to be symmetric [19]. However, the relative revolution time variation of a specific ion species is actually determined by

$$\frac{\delta T}{T} = -\left(\frac{1}{\gamma^2} - \frac{1}{\gamma_t^2}\right)\frac{\delta(B\rho)}{B\rho} = -\eta\frac{\delta(B\rho)}{B\rho}, \qquad (1)$$

where γ is the Lorentz factor of the ion, γ_t the transition point of the ring, η the so-called phase-slip factor [14], and $\delta(B\rho)$ the spread of magnetic rigidities of the ions stored in the ring.

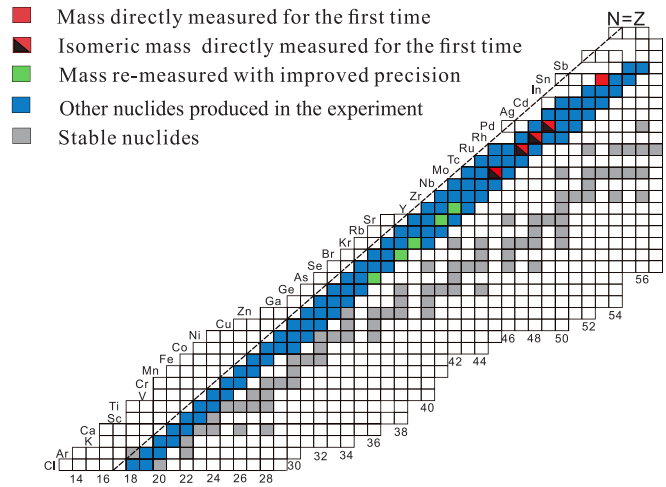

FIG. 3. Nuclei studied in the experiment reported here.

From Eq. (1), one sees that the T peak shape is affected by both the $B\rho$ distribution and η (or equivalently, γ and γ_t). In fact, the asymmetric peak shapes are commonly encountered due to the following factors:

(i) The $B\rho$ distribution could be asymmetric. This is because the nuclei of interest are produced in nuclear reaction and thus inevitably have large $B\rho$ spreads after the production target. With a limited magnetic rigidity (Bρ) acceptance of the machine, only a narrow cut from this broad distribution is injected into the ring. If a $B\rho$ distribution for one ion species is cut at its edge, the resultant $B\rho$ distribution in the ring will be asymmetric. Moreover, as the magnetic fields of CSRe are not stable during the experiment, the resultant peak shapes will be further distorted when the field instabilities are corrected [35].

(ii) η is not constant. This is partly because γ_t is orbit dependent [41,42], due to the effects of the higher order magnetic fields [43]. Furthermore, even in an ideal condition that γ_t is absolutely constant, η still varies with γ within the $B\rho$ acceptance. This means that the time peaks in the IMS are intrinsically asymmetric.

(iii) The ions with different Z will experience different energy losses when passing through the carbon foil of the TOF detector. Such energy losses could modify the shapes of the original $B\rho$ distributions of the stored ions.

To quantitate the asymmetry of T peaks, the skewness parameter [44] defined as

$$\text{skewness} = \frac{m_3}{m_2^{3/2}} \tag{2}$$

is adopted, where $m_2 = \frac{1}{n}\sum_{i=1}^{n}(T_i - \overline{T})^2$ and $m_3 = \frac{1}{n}\sum_{i=1}^{n}(T_i - \overline{T})^3$ are the second and third moments of the distribution, respectively, and $\overline{T}$ is the arithmetic mean value of n individual T_i values. The positive/negative skewness indicates a right-skewed/left-skewed distribution.

Figure 4 shows the skewnesses of the well-separated T peaks in Fig. 2. The nuclei with different isospin projections, $T_z = (N - Z)/2$, are marked with different colors. As expected, most of the peaks are not symmetric and the skewnesses of the peaks for nuclei with a given T_z gradually evolve. One can see that, although most of the peaks are right skewed, some heavier nuclei with $T_z = 1/2$, $T_z = 1$, and $T_z = 3/2$ have skewness below or close to zero. Indeed, the simulation using LISE++ [36] shows that the $B\rho$ (momentum) distributions of these heavier nuclei are different from the lighter ones.

C. Resolved peaks

To well describe the skewed peak shape and extract the mean value, the so-called EMG function [31,32] is used:

$$f(T) = \frac{h\sigma}{\tau}\sqrt{\frac{\pi}{2}}\exp\left[\frac{1}{2}\left(\frac{\sigma}{\tau}\right)^2 \pm \frac{\mu - T}{\tau}\right] \times \text{erfc}\left[\frac{1}{\sqrt{2}}\left(\frac{\sigma}{\tau} \pm \frac{\mu - T}{\sigma}\right)\right]. \tag{3}$$

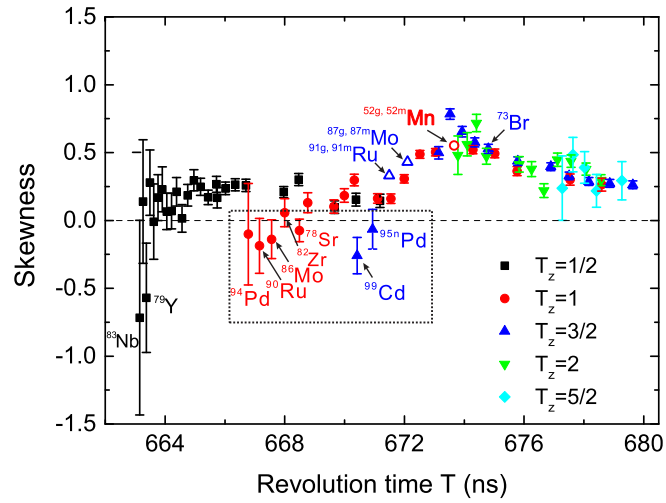

FIG. 4. Systematics of skewness parameters for the well-resolved single peaks. The symbols in different colors correspond to nuclei with different T_z. The skewnesses of ^{91g,91m}Ru, ^{87g,87m}Mo, and ^{52g,52m}Mn (open symbols) are obtained by the fitting parameters of the overlapping peaks. Some heavier nuclei with skewnesses below or close to zero are enclosed by a dotted line. ^{95n}Pd represents a long-lived high-spin isomer ($J^\pi = 21/2^+$) with excitation energy of 1875 keV [23,45].

Here, the signs "+" and "−" are used for peaks with positive and negative skewness, respectively. h, σ, and μ are the amplitude, the standard deviation, and the centroid of the unmodified Gaussian distribution, respectively. τ is the relaxation time parameter of the exponent, and $\text{erfc}(x) = \frac{2}{\sqrt{\pi}}\int_x^\infty e^{-t^2}dt$ is the complementary error function. The mean value and standard deviation of the distribution are expressed as [46]

$$\mu_T = \mu \pm \tau \quad \text{and} \quad \sigma_T = \sqrt{\sigma^2 + \tau^2}, \tag{4}$$

and the skewness is given [46] by

$$\text{skewness} = \pm\frac{2\tau^3}{(\sigma^2 + \tau^2)^{3/2}}. \tag{5}$$

The well-separated single peaks were fitted by Eq. (3) according to their skewness as shown in Fig. 4. For the apparently right-skewed peaks, the right-skewed EMG functions were used in the fitting. While for the time peaks with skewness close to zero, such as the ones enclosed in the box in Fig. 4, three functions of right-skewed EMG, left-skewed EMG, and the well known Gaussian type, were used to fit the peaks. In general, the τ parameter was not converged if the right-skewed EMG function was used to fit the peaks with negative skewness, and vice versa. Therefore, we used the right-skewed/left-skewed EMG function to fit the peaks with positive/negative skewness. The determined mean revolution times were the same within the error bars, as those using the Gaussian function. However, the fit with Gaussian function usually gave a larger χ^2_{red} value. Therefore, to keep consistency, the skewed EMG functions were used to fit all the well-resolved peaks in the subsequent analysis. We note

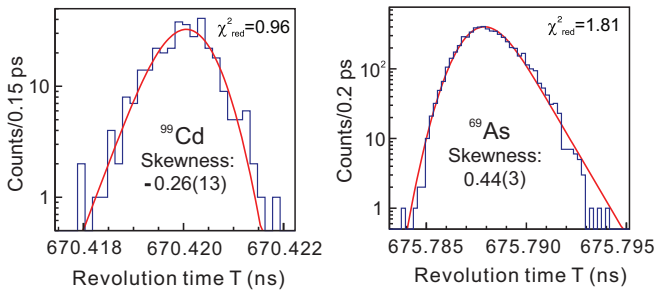

FIG. 5. Examples of fits to the left-skewed (^{99}Cd) and right-skewed (^{69}As) peaks. $\chi^2_{\rm red}$ is the reduced χ-square value of the fit.

that the mean revolution times obtained from such analysis are the same as the arithmetic mean values.

Examples of left-skewed and right-skewed peaks are shown in Fig. 5 together with the fit results indicated by red solid lines. The determination of the bin width follows the Freedman-Diaconis rule [47].

The obtained σ and τ parameters for the single peaks containing more than 300 counts are displayed in Fig. 6, where a clear systematics is established with smooth variation of σ and τ with changing T. The σ and τ were fitted by an empirical function

$$Y(T) = \sqrt{\left[\left(1 - \left(\frac{a}{T}\right)^2 - \frac{1}{b^2}\right)cT\right]^2 + d^2}, \qquad (6)$$

where Y represents σ or τ, and a, b, c, and d are free parameters. The fit curves are shown as red solid lines in Fig. 6. The fitted σ or τ values using Eq. (6) are in fact the mathematical expectations of these two parameters, and they were used as fixed parameters to fit the single peaks which have small counting statistics. Based on μ_T extracted from the peak fits,

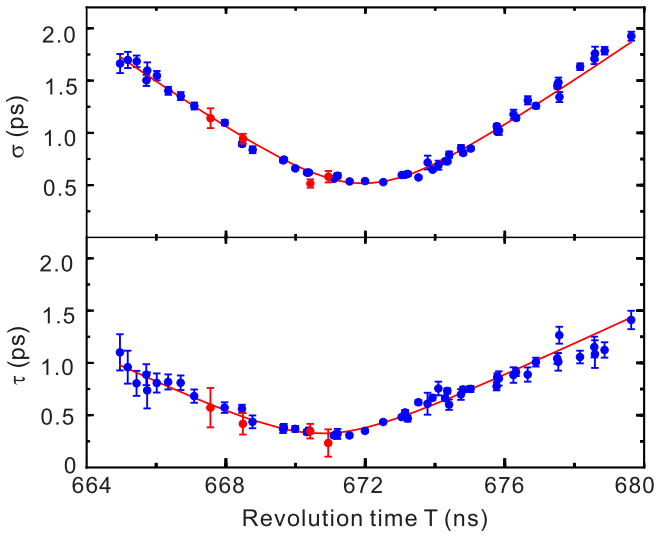

FIG. 6. The EMG function parameters σ and τ obtained from the fits applied to well-resolved peaks. The σ and τ obtained from four left-skewed peaks (^{86}Mo, ^{78}Sr, ^{99}Cd, and ^{95n}Pd from left to right) are marked in red symbols. The red solid curves show the fit results of σ and τ based on Eq. (6).

the $m/q(\mu_T)$ calibration was performed by using a third order polynomial function

$$m/q(\mu_T) = a_0 + a_1\mu_T + a_2\mu_T^2 + a_3\mu_T^3, \qquad (7)$$

where m/q is the mass-to-charge ratio of the ion species, and a_i ($i = 0, 1, 2, 3$) are free parameters to be determined from the fit. In total, 51 well-resolved peaks of nuclei with mass uncertainties of less than 10 keV in the latest Atomic Mass Evaluation (AME20) [48] (see Fig. 7 for details on these nuclei) were used in the fitting procedures via Eq. (7). Note that more precise mass values of ^{82}Zr and ^{84}Nb from JYFLTRAP [49] instead of our previous reported values [30] were adopted in AME20. The obtained a_i ($i = 0, 1, 2, 3$) parameters were then used for the mass determination.

To check the reliability of the analysis, the 51 nuclear masses have been redetermined individually by using the other 50 nuclei as calibrants. The redetermined mass excess values ($\rm ME_{exp}$) were utilized to calculate the normalized χ_n,

$$\chi_n = \sqrt{\frac{1}{N_c}\sum_{i=1}^{N_c}\frac{[\rm ME_{exp,\it i} - ME_{AME20,i}]^2}{\sigma^2_{\rm exp,\it i} + \sigma^2_{\rm AME20,\it i}}} \qquad (8)$$

with N_c being the number of nuclei, and $\rm ME_{AME20}$ the mass excess values in AME20.

The ME differences between $\rm ME_{exp}$ and $\rm ME_{AME20}$ for those nuclei are shown in Fig. 7. The differences are divided into two groups.

Figure 7(a) shows the results of 43 lighter nuclei with positive skewness. $\chi_n = 0.98$ is within the expected range of $1 \pm 1/\sqrt{2N_c} = 1 \pm 0.11$ ($N_c = 43$) at 1σ confidence level, indicating that no additional systematic error has to be considered for these nuclei.

Figure 7(b) presents the heavier nuclei with $A \geqslant 78$, $T_z = 1$ and $A \geqslant 95$, $T_z = 3/2$. Most of them have negative skewness as shown in the dashed box in Fig. 4. Different from Fig. 7(a), all the redetermined ME values shown in Fig. 7(b) are underestimated compared to the ME values in AME20, with a weighted mean deviation of -18 keV and $\chi_n = 1.8$, which is beyond the expected range of $1 \pm 1/\sqrt{2N_c} = 1 \pm 0.25$ ($N_c = 8$). In order to force $\chi_n = 1$, a systematic error of $\sigma_{\rm sys} = 19$ keV has been added to these ME values. It is noted that the mass calibration was governed by the lighter nuclei, thus the -18 keV deviation stems most probably from different shapes of $B\rho$ distributions of heavier nuclei compared to those of lighter ones. In principle, such deviation may gradually change with A, which was not clearly observed in our data due to large mass uncertainties.

It is worth mentioning that the redetermined ME values of ^{82}Zr, ^{84}Nb, and ^{90}Ru shown in Fig. 7(b) are consistent with our previous results [30], where the masses were directly determined by using arithmetic mean revolution times. The systematic deviations of ^{82}Zr, ^{84}Nb and ^{90}Ru were pointed out by the authors of Ref. [49] based on their mass measurements using the JYFLTRAP Penning-trap spectrometer. Based on the present analyses, such systematic deviations could be due to the different shapes of $B\rho$ distributions of light and heavy nuclei. Figure 8 displays the selected $\rm ME_{exp} - ME_{AME20}$ values from Fig. 7(a) for nuclei with our redetermined mass

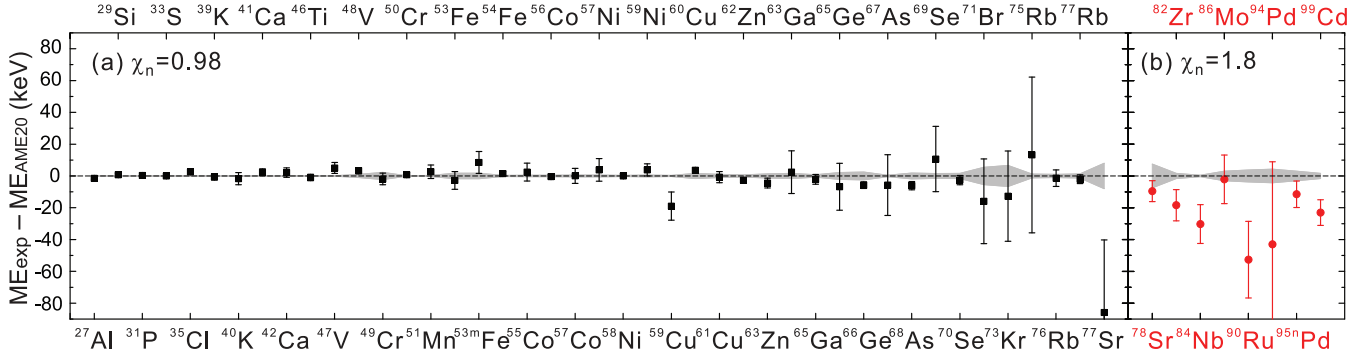

FIG. 7. The mass excess (ME) differences between this experiment (ME_{exp}) and AME20 (ME_{AME20}) for all the reference nuclei used in the mass calibration. The error bars show the uncertainty of ME_{exp} and the gray band shows the uncertainty of ME_{AME20}. The χ_n values are noted. See text for the difference between (a) and (b).

uncertainties of less than 4 keV. The projection of the mass differences is shown on the right side of the figure. There seems to be an underestimation for the heavier nuclei, such as ^{62}Zn, ^{66}Ge, and ^{68}As with $T_z = 1$. Such deviations are smaller for the $T_z = 3/2$ chain, e.g., ^{63}Zn, ^{65}Ga, and ^{77}Rb, which belong to the same T_z nuclei of interest in this work. Overall, the calculated $\chi_n = 1.08$ shows that the obtained high mass precision in Fig. 8 is justified even at an uncertainty level as low as a few keV.

In summary, by using the EMG function to fit the well-resolved peaks, the fit parameters σ and τ were determined and their variations with T were empirically established. The expected σ and τ values determined by Eq. (6) were used in deconvoluting the overlapping peaks. From the fitting procedure, we also extracted the T values which were utilized for precise mass determination. The systematic deviation of -18 keV and the systematic error of 19 keV were obtained for the heavier nuclei with $A \geqslant 78$, $T_z = 1$ and $A \geqslant 95$, $T_z = 3/2$. The extent of such deviation may depend on the specific experimental conditions. In the following mass determinations of such heavy nuclei of interest, the mass values are shifted by 18 keV and an extra systematic error of 19 keV is added quadratically to the uncertainties.

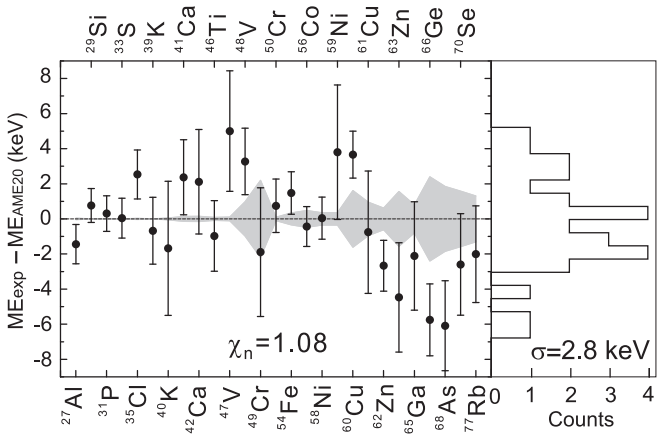

FIG. 8. Same as Fig. 7, but for nuclei with ME_{exp} uncertainties less than 4 keV.

D. Overlapping peaks

Nine examples of overlapping peaks are presented in Fig. 9. For the top five cases, the masses of ground and isomeric states are precisely known [28,50]. For the bottom four cases with $T_z = 3/2$, the masses of all ground states are known [50], but the existence or the excitation energies of the low-lying isomers are not certain. In this work, the low-lying isomers in ^{95}Pd, ^{93}Rh, and ^{87}Mo are reported for the first time.

The analyses of the overlapping peaks were performed by employing left-skewed and right-skewed EMG functions as well as Gaussian function. We used the expected σ and τ parameters according to Eq. (6) in the EMG functions. For Gaussian functions, the standard deviation parameters were fixed as $\sqrt{\sigma^2 + \tau^2}$.

The χ^2_{red} value obtained in the fitting was taken as criteria to select a proper function among the three in deconvoluting the overlapping peaks. It was found that the right-skewed EMG function is the best for fitting the overlapping peaks of ^{52g,52m}Mn, ^{87g,87m}Mo, and ^{91g,91m}Ru. For examples, when the Gaussian functions are used to fit these overlapping peaks, the χ^2_{red} values are as large as 3–12, and the obtained T values deviate by maximum 3σ from the right-skewed EMG fitting. The fit results using right-skewed EMG function are shown in Fig. 9 together with the skewnesses of the deconvoluted individual peaks. The obtained skewnesses for ^{52g,52m}Mn, ^{87g,87m}Mo, and ^{91g,91m}Ru are presented in Fig. 4 to illustrate the systematic variation. One can see that these skewness values are large, especially for ^{52g,52m}Mn. The large positive skewness indicates that the right-skewed EMG function is appropriate to deconvolute these overlapping peaks.

For overlapping peaks of ^{43g,43m}Sc, ^{74}Kr and ^{37}Ar, ^{93g,93m}Rh, ^{95g,95m}Pd, ^{97g,97m}Ag, and ^{101g,101m}In, the fits using left-skewed, right-skewed EMG functions, and Gaussian functions yielded compatible χ^2_{red} and T values. In Fig. 9, we show the adopted fit results under the condition that the χ^2_{red} value is minimum among the three fitting functions. The calculated skewness of each component is also shown. The absolute skewnesses are generally small, indicating that these individual peak shapes are actually not far from symmetric.

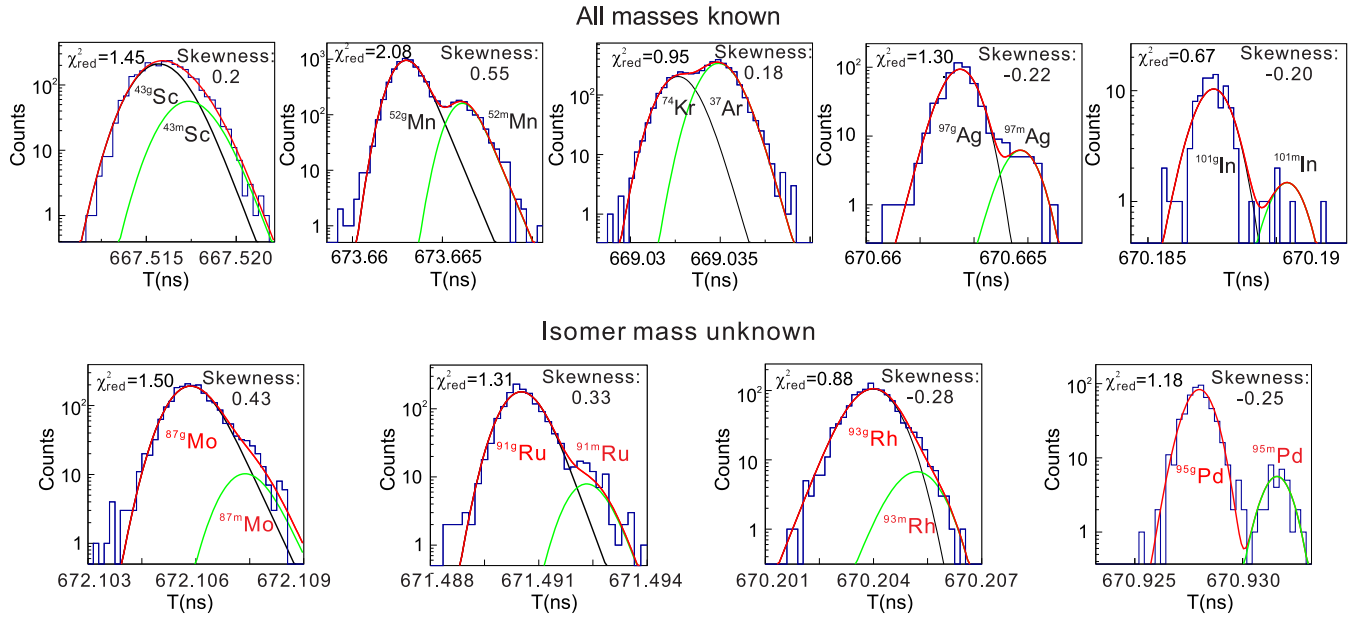

FIG. 9. The overlapping peaks of ^{43g,43m}Sc, ^{52g,52m}Mn, ^{74}Kr and ^{37}Ar, ^{97g,97m}Ag, ^{101g,101m}In, ^{87g,87m}Mo, ^{91g,91m}Ru, ^{93g,93m}Rh, and ^{95g,95m}Pd. The nuclei (isomers) shown in the top five panels have known mass values. The red curve represents an associated fitting result with double EMG functions. The black and green curves represent the corresponding deconvolution of the overlapping peaks. To show details of the tail, a logarithmic coordinate of counts is used. The $\chi^2_{\rm red}$ value of the fitting and the skewness of the deconvoluted individual peak are also noted.

Here, we note that there is no strong evidence that the peak of ^{93g,93m}Rh contains multiple components. Nevertheless, the low-lying $1/2^-$ state was predicted [51], and this state could be an isomer as systematically observed in the neighboring isotopes ^{91,95}Rh [52,53] and isotones ^{91}Tc [54], ^{95}Ag [55]. We also tried to fit the peak with two EMG functions in order to obtain the excitation energy of the hypothetical $1/2^-$ isomer. The result is regarded here as a recommended value.

After fitting the overlapping peaks, the mean revolution times of both components were determined. Then the mass values were obtained utilizing the 51 well-resolved peaks mentioned in the previous subsection for calibration. To check the validity of the deconvolution of the overlapping peaks, the redetermined MEs of some ground states and isomers were compared with the literature values in Fig. 10, where a nice agreement is observed for nuclei from ^{37}Ar to ^{91g}Ru ($T_z = 3/2$). For the heavier $T_z = 3/2$ nuclei from ^{95}Pd through ^{101}In, and also including ^{93}Rh, an upshift of 18 keV and a systematic error of 19 keV have been applied, giving reasonable agreement with literature values.

It is worth mentioning that the ground-state masses of ^{87}Mo, ^{91}Ru, ^{93}Rh, and ^{95}Pd are in good agreement with the literature values (see the red filled squares in Fig. 10), providing a strong support for the reliability of the newly obtained mass values of their isomers.

III. NEW MASSES AND DISCUSSIONS

Table II presents the new mass excesses from this work together with literature values and some relevant information. The masses of ^{69}As, ^{73}Br, ^{75}Kr, ^{79}Sr, and ^{81}Y are obtained with an improved precision comparable to that of the Penning-trap mass spectrometry, and the mass excesses of ^{103}Sn and the low-lying $1/2^-$ isomers in ^{87}Mo, ^{91}Ru, and ^{95}Pd are directly measured for the first time. The $1/2^-$ isomer in ^{93}Rh is proposed. The measured excitation energies of the isomers are given in the last column of Table II.

A. ^{69}As, ^{73}Br, ^{75}Kr, ^{79}Sr, and ^{81}Y

Our analysis yielded high precision ME values of the $T_z = 3/2$ nuclei ^{69}As, ^{73}Br, ^{75}Kr, ^{79}Sr, and ^{81}Y. All these nuclei have well-separated and right-skewed time peaks in the

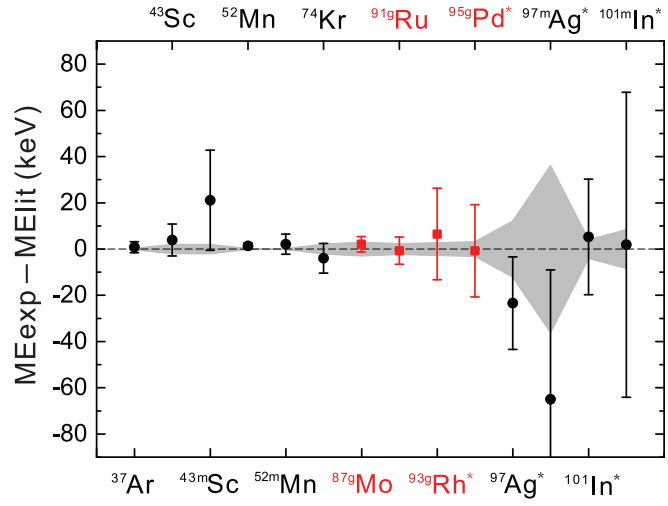

FIG. 10. ME differences between this experiment $\rm ME_{exp}$ and the literature value $\rm ME_{lit}$ taken from AME20 [48] and NUBASE2020 [50] (except for $\rm ME_{lit}$ of ^{101g,101m}In, which are taken from Ref. [28]). The error bars show the $\rm ME_{exp}$ uncertainties while the gray band illustrates the $\rm ME_{lit}$ uncertainty. The $\rm ME_{exp}$ value of the nuclei noted by "*" have been shifted up by 18(19) keV.

TABLE II. Summary of the results obtained from fitting to the single peaks and to the overlapping peaks with the expected σ and τ values defined by Eq. (6). For the overlapping peaks, the number of counts of the isomeric/ground state corresponds to the integral area of each deconvoluted component, and the σ_T and skewness are calculated according to Eqs. (4) and (5). The isomer ratio is the number of counts corresponding to the isomeric state relative to the total number of counts for this nuclide. △ ME is the ME difference between this work (ME_{exp}) and the literature value (ME_{lit}) in AME20 and NUBASE2020 [48,50]. The last column lists the measured excitation energies of the isomers, where applicable.

	Counts	σ_T(ps)	Skewness	Isomer ratio(%)	ME_{exp}(keV)	ME_{lit}(keV)	△ ME (keV)	Ex(keV)
^{69}As	6145	1.31(1)	0.44(3)	–	−63136.8(29)	−63116(22)[a]	−21(22)	–
^{73}Br	5287	1.09(1)	0.53(3)	–	−63622.9(27)[b]	−63645.8(67)	23(7)	–
^{75}Kr	5319	1.02(1)	0.58(3)	–	−64324.6(26)	−64323.6(81)	−1.0(85)	–
^{79}Sr	4011	0.84(1)	0.78(4)	–	−65474.7(26)	−65479.7(74)	5.0(79)	–
^{81}Y	2865	0.79(1)	0.50(5)	–	−65720.7(28)	−65712.9(54)	−7.8(61)	–
^{103}Sn	23(6)	0.78	−0.18	–	−67138(68)[c,d]	−67092(100)#[e]	−46(121)	–
^{87g}Mo	1957(44)	0.65	0.43	–	−66883.0(33)	−66884.8(29)	1.8(44)	–
^{87m}Mo	103(10)	0.65	0.43	5.0(5)	−66573(30)	–	–	310(30)
^{91g}Ru	1357(37)	0.63	0.33	–	−68241.0(59)	−68239.8(22)	−1.2(63)	–
^{91m}Ru	70(8)	0.63	0.33	4.9(6)	−67809(30)	−68580(500)	771(501)	432(31)
^{93g}Rh	1081(33)	0.64	−0.28	–	−69006(20)[d]	−69011.8(26)	6(20)	–
^{93m}Rh	69(8)	0.64	−0.28	6.0(7)	−68739(44)[d,f]	–	–	267(48)[f]
^{95g}Pd	521(23)	0.66	−0.25	–	−69967(20)[d]	−69965.9(30)	−1(20)	–
^{95m}Pd	35(6)	0.66	−0.25	6.3(11)	−69163(33)[d]	–	–	804(39)

[a]Adopted from Ref. [56].
[b]Corresponding mainly to the $5/2^-$ isomer at an excitation energy of 26.9 keV. See text for details.
[c]The peak is fitted by left-skewed EMG function with σ and τ parameters fixed as the expected values.
[d]ME values are shifted up by 18 keV.
[e]Extrapolated ME value in AME20.
[f]Recommended values, see text for details.

revolution time spectrum of Fig. 2. A comparison of our ME values with the literature ones is presented in Fig. 11.

The mass of ^{69}As was indirectly measured via the endpoint energy of β^+ decay of ^{69}As and ^{69}Se [57,58]. The average ME value was −63110(30) keV [48]. Recently, the mass of ^{69}As was directly measured by the MR-TOF-MS at the FRS Ion Cather at GSI to be −63116(22) keV [56]. Our newly-measured ME value of −63136.8(29) keV is in agreement with both values, but the precision is improved by almost an order of magnitude. The masses of ^{75}K, ^{79}Sr, and ^{81}Y were measured by Penning-trap mass spectrometry [59–61]. Our remeasured ME values are in good agreement with these measurements.

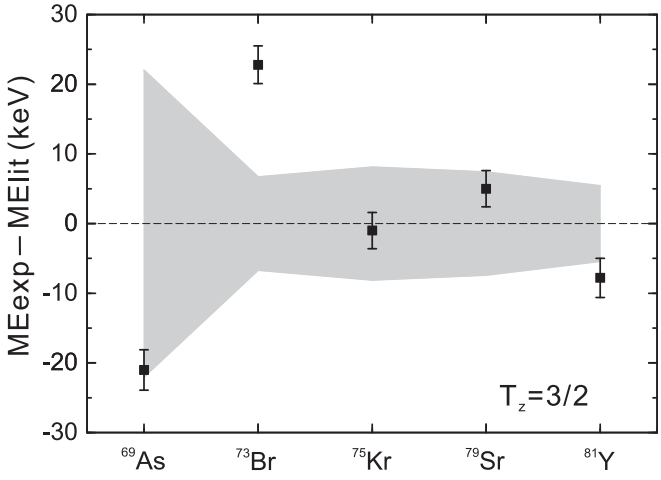

FIG. 11. ME differences between this experiment (ME_{exp}) and the literature values (ME_{lit}) from Ref. [56] for ^{69}As, and from AME20 for ^{73}Br, ^{75}Kr, ^{79}Sr, and ^{81}Y. The error bar shows the ME_{exp} uncertainty while the gray band shows the ME_{lit} uncertainty.

The mass of ^{73}Br was measured by several methods, such as the measurement of mass ratio of ^{73}Br and ^{72}Br at the Chalk River On-Line Isotope Separator [62], the measurement of the β-decay end-point energy at the Wright Nuclear Structure Laboratory [63], the isochronous mass measurements at the ESR [64], the Penning-trap as well as the MR-TOF mass measurements at ISOLTRAP [65,66]. Among those measurements, the Penning-trap mass measurement gives the smallest uncertainty of 7 keV and makes the largest contribution to the AME20 value of ME = −63646(7) keV.

In this work, the ME value of ^{73}Br is determined to be −63622.9(27) keV, which is more precise but deviates by more than 3σ from the AME20 value, as shown in Fig. 11. This discrepancy can be interpreted if the existence of an isomer in ^{73}Br is assumed.

In fact, most of the ^{73}Br primary fragments produced in the projectile fragmentation of ^{112}Sn are in highly excited states, and they mainly decay to the low-lying $5/2^-$ state at $E_x = 26.9$ keV [67]. For the neutral atom, this state de-excites to the $1/2^-$ ground state via the $E2$ γ + IC (internal conversion) transition. However, the ions stored in CSRe are fully stripped at relativistic energies, and thus the IC decay path is completely blocked. Such cases were extensively studied in the storage ring ESR [68,69]. Consequently, the ^{73}Br ions at $E_x = 26.9$ keV level have a longer lifetime in CSRe. Indeed,

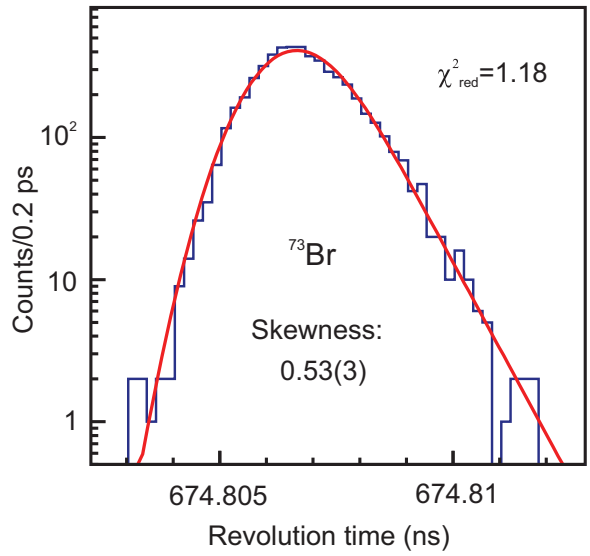

FIG. 12. The peak of ^{73}Br fitted by the right-skewed EMG function with the expected σ and τ parameters according to Eq. (6).

the lifetime of the $E_x = 26.9$ keV level was estimated to be $1.4\ \mu s \leqslant \tau \leqslant 9.1\ \mu s$ [70]. The conversion coefficient for such a low-energy transition was calculated to be 103.6 [71], leading to a partial γ-decay lifetime of $146\ \mu s \leqslant \tau \leqslant 952\ \mu s$. So the bare ^{73}Br ions in the $E_x = 26.9$ keV state have a lifetime long enough to be measured in CSRe. The time peak of ^{73}Br may thus correspond to the mixture of both, the ground and the $E_x = 26.9$ keV excited, states.

Our measured ME is 23(7)-keV larger than the ground-state ME value of ^{73}Br recommended in AME20, indicating that, if our hypothesis is correct, the ^{73}Br ions at $E_x = 26.9$ keV significantly contribute to the time peak of ^{73}Br shown in Fig. 12. Indeed, the skewness value of 0.53(3) well follows the systematics shown in Fig. 4, and a single peak fitting with expected σ and τ values gives a $\chi^2_{red} = 1.18$, indicating that right-skewed EMG function can well describe the peak shape. As the ground state and the isomer are too close to be resolved, a simple estimate using the literature mass values yields 85(27)% and 15(27)% contributions from the $E_x = 26.9$ keV level and the ground state, respectively. Our measurement validates that the $5/2^-$ level at $E_x = 26.9$ keV is indeed an isomer with a half-life in the order of microseconds.

B. ^{103}Sn

Combining the measured Q_{EC} value (7.64 ± 0.07 MeV [72]) and the mass of ^{103}In, the ME of ^{103}Sn was reported to be −66970(70) keV in the AME16 [73]. However, this ME value was not adopted in AME20 since it breaks the smoothness of the mass surface in this region. Instead, an estimated ME value of −67090(100) keV was recommended [48]. In the present work, the mass of ^{103}Sn is directly measured for the first time, and the determined ME value of −67138(68) keV is in good agreement with the extrapolated value in AME20. It is worth noting that the new mass value of ^{103}Sn supports strongly the zigzag pattern of $\Delta_{3n}(Z, N)$ presented in Fig. 3(b) of Ref. [28].

TABLE III. ME values derived using the new ME of ^{103}Sn from this work. # indicates an extrapolated ME value in AME20 [48].

	ME_{exp}(keV)	ME_{AME20}(keV)
^{104}Sb	−59340(70)	−59300(100)#
^{107}Te	−60700(70)	−60660(100)#
^{108}I	−52820(70)	−52770(100)#
^{111}Xe	−54570(90)	−54520(120)#
^{112}Cs	−46460(90)	−46420(120)#

Based on the ME value of ^{103}Sn measured in this work, as well as the literature values of Q_p (for ^{108}I) and Q_α (for ^{107}Te, ^{108}I, ^{111}Xe, and ^{112}Cs) from Ref. [48], the mass excesses of ^{104}Sb, ^{107}Te, ^{108}I, ^{111}Xe, and ^{112}Cs are derived and given in Table III. Note that these mentioned Q values were precisely measured and reported in Refs. [74–77].

C. ^{87m}Mo, ^{91m}Ru, ^{93m}Rh, and ^{95m}Pd

The masses of the ground states of ^{87}Mo, ^{91}Ru, ^{93}Rh, and ^{95}Pd were precisely measured by Penning-trap mass spectrometry such as CPT, SHIPTRAP, and (or) JYFLTRAP with mass precision of a few keV [23–25,78]. These mass values were adopted in AME20 [48]. Our mass values agree well with AME20 as shown in Fig. 10.

All these nuclei are expected to have low-lying $1/2^-$ isomers. The low-lying $1/2^-$ isomer in ^{91}Ru with a half-life of 7.6 s has been observed in the measurement of β-delayed protons of ^{91m}Ru [79], while those in ^{87}Mo, ^{93}Rh, and ^{95}Pd have not been found in spectroscopy experiments to date. Therefore, the low-lying isomers discovered in this work are assigned as $1/2^-$.

In the Penning-trap mass measurements, these low-spin states were not observed probably because either the low-spin states are less favorably produced in the employed nuclear reactions, or their half-lives are too short to be detected. Here we note, that typically singly charged ions were used in these measurements. In the projectile fragmentation reaction, a sizable population of low-spin isomers is expected [80], and the fast measurement using the present IMS technique allows observation of such isomers.

The ME values of the isomeric states in ^{87}Mo and ^{93}Rh are determined in this work to be −66573(30) keV and −68739(44) keV, yielding the excitation energies of 310(30) keV and 267(48) keV, respectively. The ME of the $1/2^-$ low-lying isomer in ^{95}Pd is measured to be −69163(33) keV, yielding an excitation energy of 804(39) keV. We note that this is now the lowest excited state known in ^{95}Pd [67].

Previously, the lower limit of $Q_{EC} - Q_p$ value deduced from the β-delayed proton decay of ^{91m}Ru to ^{90}Mo was 4.3 MeV [79]. Combining the well-known mass of ^{90}Mo, the ME of ^{91m}Ru was evaluated to be −68580(500) keV [50]. Based on the ground-state mass of ^{91}Ru precisely measured by JYFLTRAP and SHIPTRAP [23] and CPT [24], the excitation energy of the isomer was reported to be −340(500) keV in NUBASE2020 [50].

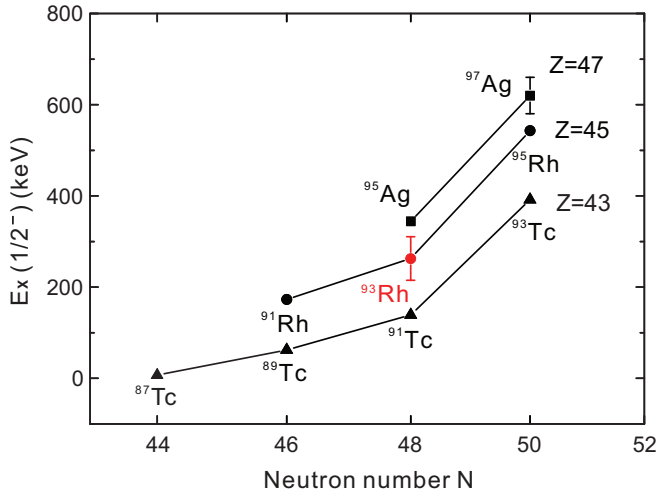

FIG. 13. Excitation energies of the $1/2^-$ isomers in odd-Z Tc, Rh, and Ag isotopes as a function of N. The filled red circle is the recommended excitation energy of the $1/2^-$ isomer in ^{93}Rh. The solid lines are to guide the eye.

In the present experiment, the ME of the $1/2^-$ isomer in ^{91}Ru is directly measured to be $-67809(30)$ keV, which is 771(501) keV less bound than the evaluated value [50]. The excitation energy of ^{91m}Ru is thus determined to be 432(31) keV. This value is an order of magnitude more precise than the NUBASE2020 value.

The systematics of excitation energies of the $1/2^-$ isomers are shown in Figs. 13 and 14. One sees that the newly determined excitation energies of the $1/2^-$ isomers in ^{95}Pd, ^{93}Rh, ^{87}Mo, and ^{91}Ru fit well into the systematics, which also supports our recommended mass excess of the $1/2^-$ isomer in ^{93}Rh.

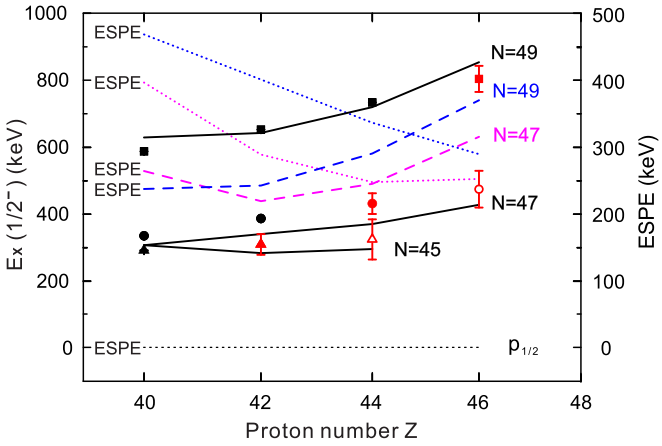

FIG. 14. Excitation energies of the $1/2^-$ isomers in the nuclei with N or Z close to 50 (left axis), and effective single-particle energies (ESPEs) of $\nu 1g_{9/2}$ relative to $\nu 2p_{1/2}$ as a function of Z for $N = 47,\ 49$ isotones from the shell model calculation (right axis). The excitation energies measured in this work are indicated by filled red symbols. The extrapolated excitation energies following the systematics are indicated by open red symbols. The excitation energies obtained from the shell model calculation are denoted by solid lines (see text for details). The dotted/dashed lines show the ESPE results without/with the tensor forces included in the shell model calculation.

D. $E_x(1/2^-)$ systematics and impact of tensor forces on shell gap evolution

The ground states of odd-A nuclei close to the $N = Z = 50$ shell closure are typically in $1g_{9/2}$ configuration with $J^\pi = 9/2^+$. If a nucleon (neutron or proton) is promoted from $2p_{1/2}$ into $1g_{9/2}$ orbit, a low-lying $2p_{1/2}^{-1}$ hole state with $J^\pi = 1/2^-$ is formed. Such states are systematically observed as long-lived isomers in this region because of the slow $1/2^- \rightarrow 9/2^+$ $M4$ transition. Therefore, the new isomers in ^{95}Pd, ^{91}Ru, and ^{87}Mo identified in the present work are assigned as the $1/2^-$ neutron-hole states, and the isomer in ^{93}Rh is assigned as the $1/2^-$ proton-hole state.

Figure 14 shows the excitation energy systematics of the $1/2^-$ neutron-hole states, $E_x(1/2^-)$. The red filled symbols indicate the newly measured values. Regular behavior is observed, and thus the $E_x(1/2^-)$ values are extrapolated to neighboring nuclei (red open symbols) where no experimental information is available. One sees that $E_x(1/2^-)$ is the smallest for the $N = 45$ isotones and increases if a pair of neutrons is added within an isotopic chain. Similarly, $E_x(1/2^-)$ increases gradually by adding a pair of protons within an isotonic chain. Considering the neutron-hole character of the $J^\pi = 1/2^-$ states, the excitation energies of such isomers are directly related to the $p_{1/2}$-$g_{9/2}$ shell gap, i.e., the energy difference between the $\nu 2p_{1/2}$ and $\nu 1g_{9/2}$ neutron orbits. Therefore the systematics in Fig. 14 illustrates the gap evolution.

It is well known that the monopole part of the proton-neutron (p-n) interaction plays a decisive role in the shell evolution [81,82]. Apart from the central component of the interaction which is always attractive, the tensor force is attractive only if protons occupy the spin-up ($j = l + 1/2$) single particle orbits and neutrons occupy the spin-down ($j' = l' - 1/2$) orbits, or vice versa. The tensor force is repulsive when both protons and neutrons simultaneously occupy either spin-down or spin-up orbits. Such character of the tensor force leads to the relative shifts of single particle orbits when protons or neutrons are added to nuclei. For example, the emergence of the new magic number at $N = 34$ has been interpreted based on this scenario of the tensor interactions [83].

In the present case, the systematics shown in Fig. 14 can be qualitatively understood in a similar way. Adding proton/neutron pairs to the $\pi 1g_{9/2}/\nu 1g_{9/2}$ orbit increases the repulsive tensor force between the protons and neutrons in the $1g_{9/2}$ single particle orbits. This results in a larger gap between the $\nu 2p_{1/2}$ and the $\nu 1g_{9/2}$ neutron orbits. Consequently, the $E_x(1/2^-)$ of neutron-hole states increases with Z/N within an isotonic/isotopic chain.

To get more insight into the microscopic origin of the $p_{1/2}$-$g_{9/2}$ neutron shell gap evolution and the impact of the tensor force in this region, dedicated shell-model calculations were performed using the KSHELL code [84] with the state-of-the-art monopole-based universal interaction $V_{\rm MU}$ plus a

spin-orbit force from M3Y($V_{\rm MU}$ + LS) [85,86]. The $V_{\rm MU}$ interaction consists of a Gaussian central force and a tensor force [86] and has been successfully applied to describe the shell structure of exotic nuclei in various regions [81,82,87–89]. In our calculations, the model space for both valence protons and neutrons consists of $1f_{5/2}$, $2p_{3/2}$, $2p_{1/2}$, and $1g_{9/2}$ orbitals, and ^{56}Ni is taken as an inert core. The single-particle energies were tuned such to give a consistent $E_x(1/2^-)$ value for observed odd-A systems near ^{100}Sn. The calculated excitation energies of the $1/2^-$ isomers well reproduce the experiment and are shown in Fig. 14 as solid lines.

Also shown in Fig. 14 are the $\nu 1g_{9/2}$ neutron effective single-particle energies (ESPEs) relative to $\nu 2p_{1/2}$ as a function of Z for $N = 47$ and 49 isotones (see the dotted and dashed lines). By disabling the tensor forces (dotted lines), the theoretical $p_{1/2}$-$g_{9/2}$ neutron shell gap decreases with Z. The overall effect of the tensor forces mentioned above makes the $p_{1/2}$-$g_{9/2}$ neutron shell gap to increase, if more proton pairs are added (dashed lines). This trend is consistent with the systematic variation of $E_x(1/2^-)$ shown in Fig. 14. We note, that many-body correlations beyond the simplified single-particle scheme also contribute to the $E_x(1/2^-)$ variations.

IV. CONCLUSIONS

Isochronous mass measurements of relativistic ^{112}Sn projectile fragments have been performed at CSRe in Lanzhou. An exponentially modified Gaussian function was introduced to describe the skewed revolution time distributions of stored ions and to deconvolute the overlapping time peaks. Accurate mean revolution times were extracted and used for mass determinations. The mass excesses of the low-lying $1/2^-$ isomers were directly measured in ^{87}Mo, ^{91}Ru, and ^{95}Pd and recommended in ^{93}Rh. Improved masses of ^{69}As, ^{73}Br, ^{75}Kr, ^{79}Sr, and ^{81}Y were obtained achieving a precision comparable to that of Penning-trap mass spectrometry. Further, the mass of ^{103}Sn was directly measured which enabled the indirect determination of the previously unknown masses of ^{104}Sb, ^{107}Te, ^{108}I, ^{111}Xe, and ^{112}Cs by using the experimental proton and/or α decay energies. Systematic trends of the excitation energies of the $J^\pi = 1/2^-$ isomers in $N = 47$ and 49 isotones were investigated by utilizing the state-of-the-art shell model calculations. It was found that the inclusion of the tensor force is crucial to reproduce the systematic trends of $E_x(1/2^-)$ as a function of Z.

It has been found that for measured nuclei with $T_z = 1$ and 3/2, some nuclear masses are systematically underestimated and require an appropriate correction. This is motivated by the fact that most of the peaks used for the mass calibration may have different $B\rho$ (momentum) distributions. To avoid such deviations, a new technique, the so-called $B\rho$-defined IMS [90], will be employed in the future IMS measurements. Using this new technique, both the revolution time and velocity will be simultaneously measured for each individual ions [91]. Subsequently, the experimental revolution time can be corrected to the one for a chosen magnetic rigidity or equivalently orbit length. As a result, the mass deviations due to the possible different $B\rho$ distributions are expected to be negligible.

ACKNOWLEDGMENTS

The authors thank the staff of the accelerator division of IMP for providing a stable beam. This work is supported in part by the National Key R&D Program of China (Grant No. 2018YFA0404401), the Strategic Priority Research Program of Chinese Academy of Sciences (Grant No. XDB34000000), and the NSFC (Grants No. 12135017, No. 12121005, No. 11905261, No. 11905259, and No. 11975280). Y.M.X. and X.X. acknowledge the support from the Youth Innovation Promotion Association of Chinese Academy of Sciences (Grants No. 2021419 and No. 2022423). C.X.Y. acknowledges Guangdong Major Project of Basic and Applied Basic Research (Grant No. 2021B0301030006). R.J.C. is supported by the International Postdoctoral Exchange Fellowship Program 2017 by the Office of China Postdoctoral Council (No. 60 Document of OCPC, 2017). Y.A.L. is supported by the European Research Council (ERC) under the European Union's Horizon 2020 research and innovation programme (Grant No. 682841 "ASTRUm").

[1] T. Yamaguchi, H. Koura, Y. A. Litvinov, and M. Wang, Prog. Part. Nucl. Phys. **120**, 103882 (2021).
[2] P. Walker and Z. Podolyák, Phys. Scr. **95**, 044004 (2020).
[3] M. A. Bentley and S. M. Lenzi, Prog. Part. Nucl. Phys. **59**, 497 (2007).
[4] G. W. Misch, S. K. Ghorui, P. Banerjee, Y. Sun, and M. R. Mumpower, Astroph. J. **252**, 2 (2021).
[5] M. Arnould and S. Goriely, Prog. Part. Nucl. Phys. **112**, 103766 (2020).
[6] A. Kankainen, Y. N. Novikov, M. Oinonen, L. Batist, V. V. Elomaa, T. Eronen, J. Hakala, A. Jokinen, P. Karvonen, M. Reponen, J. Rissanen, A. Saastamoinen, G. Vorobjev, C. Weber, and J. Äystö, Eur. Phys. J. A **48**, 49 (2012).
[7] Y. Sun, M. Wiescher, A. Aprahamian, and J. Fisker, Nucl. Phys. A **758**, 765 (2005).
[8] R. A. Ward and W. A. Fowler, Astrophys. J. **238**, 266 (1980).
[9] Z. Meisel, J. Phys.: Conf. Ser. **1668**, 012026 (2020).
[10] J. Dilling, K. Blaum, M. Brodeur, and S. Eliseev, Annu. Rev. Nucl. Part. Sci. **68**, 45 (2018).
[11] W. R. Plaß, T. Dickel, and C. Scheidenberger, Int. J. Mass Spectrom. **349–350**, 134 (2013).
[12] M. Z. Sun, X. H. Zhou, M. Wang, Y. H. Zhang, and Y. A. Litvinov, Front. Phys. **13**, 132112 (2018).
[13] M. Steck and Y. A. Litvinov, Prog. Part. Nucl. Phys. **115**, 103811 (2020).
[14] M. Hausmann, F. Attallah, K. Beckert, F. Bosch, A. Dolinskiy, H. Eickhoff, M. Falch, B. Franczak, B. Franzke, H. Geissel, T. Kerscher, O. Klepper, H.-J. Kluge, C. Kozhuharov, K. E. G. Löbner, G. Münzenberg, F. Nolden, Y. N. Novikov, T. Radon, H. Schatz *et al.*, Nucl. Instrum. Methods Phys. Res. A **446**, 569 (2000).

[15] M. Wang, H. S. Xu, J. W. Xia, X. L. Tu, R. S. Mao, Y. J. Yuan, Z. G. Hu, Y. Liu, H. B. Zhang, Y. D. Zang, T. C. Zhao, X. Y. Zhang, F. Fu, J. C. Yang, L. J. Mao, C. Xiao, G. Q. Xiao, H. W. Zhao, and W. L. Zhan, Int. J. Mod. Phys. E **18**, 352 (2009).

[16] H. F. Li, S. Naimi, T. M. Sprouse, M. R. Mumpower, Y. Abe, Y. Yamaguchi, D. Nagae, F. Suzaki, M. Wakasugi, H. Arakawa, W. B. Dou, D. Hamakawa, S. Hosoi, Y. Inada, D. Kajiki, T. Kobayashi, M. Sakaue, Y. Yokoda, T. Yamaguchi, R. Kagesawa *et al.*, Phys. Rev. Lett. **128**, 152701 (2022).

[17] C. Y. Fu, Y. H. Zhang, M. Wang, X. H. Zhou, Y. A. Litvinov, K. Blaum, H. S. Xu, X. Xu, P. Shuai, Y. H. Lam, R. J. Chen, X. L. Yan, X. C. Chen, J. J. He, S. Kubono, M. Z. Sun, X. L. Tu, Y. M. Xing, Q. Zeng, X. Zhou *et al.*, Phys. Rev. C **102**, 054311 (2020).

[18] X. Xu, M. Wang, K. Blaum, J. D. Holt, Y. A. Litvinov, A. Schwenk, J. Simonis, S. R. Stroberg, Y. H. Zhang, H. S. Xu, P. Shuai, X. L. Tu, X. H. Zhou, F. R. Xu, G. Audi, R. J. Chen, X. C. Chen, C. Y. Fu, Z. Ge, W. J. Huang *et al.*, Phys. Rev. C **99**, 064303 (2019).

[19] Y. H. Zhang, P. Zhang, X. H. Zhou, M. Wang, Y. A. Litvinov, H. S. Xu, X. Xu, P. Shuai, Y. H. Lam, R. J. Chen, X. L. Yan, T. Bao, X. C. Chen, H. Chen, C. Y. Fu, J. J. He, S. Kubono, D. W. Liu, R. S. Mao, X. W. Ma *et al.*, Phys. Rev. C **98**, 014319 (2018).

[20] P. Zhang, X. Xu, P. Shuai, R. J. Chen, X. L. Yan, Y. H. Zhang, M. Wang, Yu. A. Litvinov, K. Blaum, H. S. Xu, T. Bao, X. C. Chen, H. Chen, C. Y. Fu, J. J. He, S. Kubono, Y. H. Lam, D. W. Liu, R. S. Mao, X. W. Ma *et al.*, Phys. Lett. B **767**, 20 (2017).

[21] R. Knöbel, M. Diwisch, H. Geissel, Y. A. Litvinov, Z. Patyk, W. R. Plass, C. Scheidenberger, B. Sun, H. Weick, F. Bosch, D. Boutin, L. Chen, C. Dimopoulou, A. Dolinskii, B. Franczak, B. Franzke, M. Hausmann, C. Kozhuharov, J. Kurcewicz, S. A. Litvinov *et al.*, Eur. Phys. J. A **52**, 138 (2016).

[22] R. Knöbel, M. Diwisch, F. Bosch, D. Boutin, L. Chen, C. Dimopoulou, A. Dolinskii, B. Franczak, B. Franzke, H. Geissel, M. Hausmann, C. Kozhuharov, J. Kurcewicz, S. A. Litvinov, G. Martinez-Pinedo, M. Matoš, M. Mazzocco, G. Münzenberg, S. Nakajima, C. Nociforo *et al.*, Phys. Lett. B **754**, 288 (2016).

[23] C. Weber, V.-V. Elomaa, R. Ferrer, C. Fröhlich, D. Ackermann, J. Äystö, G. Audi, L. Batist, K. Blaum, M. Block, A. Chaudhuri, M. Dworschak, S. Eliseev, T. Eronen, U. Hager, J. Hakala, F. Herfurth, F. P. Heßberger, S. Hofmann, A. Jokinen, A. Kankainen *et al.*, Phys. Rev. C **78**, 054310 (2008).

[24] J. Fallis, J. A. Clark, K. S. Sharma, G. Savard, F. Buchinger, S. Caldwell, A. Chaudhuri, J. E. Crawford, C. M. Deibel, S. Gulick, A. A. Hecht, D. Lascar, J. K. P. Lee, A. F. Levand, G. Li, B. F. Lundgren, A. Parikh, S. Russell, M. Scholte-van de Vorst, N. D. Scielzo, R. E. Segel *et al.*, Phys. Rev. C **84**, 045807 (2011).

[25] E. Haettner, D. Ackermann, G. Audi, K. Blaum, M. Block, S. Eliseev, T. Fleckenstein, F. Herfurth, F. P. Heßberger, S. Hofmann, J. Ketelaer, J. Ketter, H.-J. Kluge, G. Marx, M. Mazzocco, Y. N. Novikov, W. R. Plaß, S. Rahaman, T. Rauscher, D. Rodríguez *et al.*, Phys. Rev. Lett. **106**, 122501 (2011).

[26] K. Blaum, Phys. Rep. **425**, 1 (2006).

[27] C. Hornung, D. Amanbayev, I. Dedes, G. Kripko-Koncz, I. Miskun, N. Shimizu, S. Ayet San Andrés, J. Bergmann, T. Dickel, J. Dudek, J. Ebert, H. Geissel, M. Górska, H. Grawe, F. Greiner, E. Haettner, T. Otsuka, W. R. Plaß, S. Purushothaman, A.-K. Rink, C. Scheidenberger *et al.*, Phys. Lett. B **802**, 135200 (2020).

[28] M. Mougeot, D. Atanasov, J. Karthein, R. N. Wolf, P. Ascher, K. Blaum, K. Chrysalidis, G. Hagen, J. D. Holt, W. J. Huang, G. R. Jansen, I. Kulikov, Y. A. Litvinov, D. Lunney, V. Manea, T. Miyagi, T. Papenbrock, L. Schweikhard, A. Schwenk, T. Steinsberger *et al.*, Nat. Phys. **17**, 1099 (2021).

[29] X. Xu, J. H. Liu, C. X. Yuan, Y. M. Xing, M. Wang, Y. H. Zhang, X. H. Zhou, Y. A. Litvinov, K. Blaum, R. J. Chen, X. C. Chen, C. Y. Fu, B. S. Gao, J. J. He, S. Kubono, Y. H. Lam, H. F. Li, M. L. Liu, P. Shuai, M. Si *et al.*, Phys. Rev. C **100**, 051303(R) (2019).

[30] Y. M. Xing, K. A. Li, Y. H. Zhang, X. H. Zhou, M. Wang, Y. A. Litvinov, K. Blaum, S. Wanajo, S. Kubono, G. Martínez-Pinedo, A. Sieverding, R. J. Chen, P. Shuai, C. Y. Fu, X. L. Yan, W. J. Huang, X. Xu, X. D. Tang, H. S. Xu, T. Bao *et al.*, Phys. Lett. B **781**, 358 (2018).

[31] Y. Kalambet, Y. Kozmin, K. Mikhailova, I. Nagaev, and P. Tikhonov, J. Chemometr. **25**, 352 (2011).

[32] S. Purushothaman, S. A. S. Andrés, J. Bergmann, T. Dickel, J. Ebert, H. Geissel, C. Hornung, W. R. Plass, C. Rappold, C. Scheidenberger, Y. K. Tanaka, and M. I. Yavor, Int. J. Mass Spectrom. **421**, 245 (2017).

[33] W. L. Zhan, H. S. Xu, G. Q. Xiao, J. W. Xia, H. W. Zhao, Y. J. Yuan, and H.-C. Grp, Nucl. Phys. A **834**, 694c (2010).

[34] X. L. Yan, Ph.D thesis, University of Chinese Academy of Sciences (2014).

[35] Y. M. Xing, Y. H. Zhang, M. Wang, Y. A. Litvinov, R. J. Chen, X. C. Chen, C. Y. Fu, H. F. Li, P. Shuai, M. Si, M. Z. Sun, X. L. Tu, Q. Wang, H. S. Xu, X. Xu, X. L. Yan, J. C. Yang, Y. J. Yuan, Q. Zeng, P. Zhang *et al.*, Nucl. Instrum. Methods Phys. Res. A **941**, 162331 (2019).

[36] O. B. Tarasov and D. Bazin, Nucl. Instrum. Methods Phys. Res. B **266**, 4657 (2008).

[37] J. H. Liu, X. Xu, P. Zhang, P. Shuai, X. L. Yan, Y. H. Zhang, M. Wang, Y. A. Litvinov, H. S. Xu, K. Blaum, T. Bao, H. Chen, X. C. Chen, R. J. Chen, C. Y. Fu, D. W. Liu, W. W. Ge, R. S. Mao, X. W. Ma, M. Z. Sun *et al.*, Nucl. Instrum. Methods Phys. Res. B **463**, 138 (2020).

[38] B. Mei, X. L. Tu, M. Wang, H. S. Xu, R. S. Mao, Z. G. Hu, X. W. Ma, Y. J. Yuan, X. Y. Zhang, P. Geng, S. A. Peng, Y. D. Zang, S. W. Tang, P. Ma, W. Lu, X. S. A. Yan, J. W. Xia, G. Q. Xiao, Z. Y. Guo, H. B. Zhang *et al.*, Nucl. Instrum. Methods Phys. Res. A **624**, 109 (2010).

[39] R. J. Chen, M. Wang, X. L. Yan, Q. Yang, Y. H. Lam, L. Yang, and Y. H. Zhang, Comput. Phys. Commun. **221**, 216 (2017).

[40] X. L. Tu, M. Wang, Y. A. Litvinov, Y. H. Zhang, H. S. Xu, Z. Y. Sun, G. Audi, K. Blaum, C. M. Du, W. X. Huang, Z. G. Hu, P. Geng, S. L. Jin, L. X. Liu, Y. Liu, B. Mei, R. S. Mao, X. W. Ma, H. Suzuki, P. Shuai *et al.*, Nucl. Instrum. Methods Phys. Res. A **654**, 213 (2011).

[41] M. Zhang, Y. H. Zhang, M. Wang, X. Zhou, Y. J. Yuan, X. L. Yan, Y. M. Xing, C. Y. Fu, R. J. Chen, X. Xu, P. Shuai, Q. Zeng, M. Z. Sun, H. F. Li, M. Si, Q. Wang, T. Bao, H. Y. Deng, M. Z. Liu, T. Liao *et al.*, Nucl. Instrum. Methods Phys. Res. A **1027**, 166329 (2022).

[42] R. J. Chen, X. L. Yan, W. W. Ge, Y. J. Yuan, M. Wang, M. Z. Sun, Y. M. Xing, P. Zhang, C. Y. Fu, P. Shuai, X. Xu, Y. H. Zhang, T. Bao, X. C. Chen, X. J. Hu, W. J. Huang, H. F. Li, J. H. Liu, Y. A. Livinov, S. A. Livinov *et al.*, Nucl. Instrum. Methods Phys. Res. A **898**, 111 (2018).

[43] W. W. Ge, Y. J. Yuan, J. C. Yang, R. J. Chen, X. L. Yan, H. Du, Z. S. Li, J. Yang, D. Y. Yin, L. J. Mao, X. N. Li, W. H. Zheng, G. D. Shen, B. Wu, S. Ruan, G. Wang, H. Zhao, M. Wang, M. Z. Sun, Y. M. Xing *et al.*, Nucl. Instrum. Methods Phys. Res. A **908**, 388 (2018).

[44] J. C. W. Rayner, D. J. Best, and K. L. Mathews, Commun. Stat-Theor. M **24**, 593 (1995).

[45] E. Nolte and H. Hick, Phys. Lett. B **97**, 55 (1980).

[46] J. Olivier and M. M. Norberg, Int. J. Psychol. Res. **3**, 68 (2010).

[47] D. Freedman and P. Diaconis, Z. Wahrscheinlichkeitstheorie Verw. Gebiete **57**, 453 (1981).

[48] M. Wang, W. J. Huang, F. G. Kondev, G. Audi, and S. Naimi, Chinese Phys. C **45**, 030003 (2021).

[49] M. Vilén, A. Kankainen, P. Baoczyk, L. Canete, J. Dobaczewski, T. Eronen, S. Geldhof, A. Jokinen, M. Konieczka, J. Kostensalo, I. D. Moore, D. A. Nesterenko, H. Penttilä, I. Pohjalainen, M. Reponen, S. Rinta-Antila, A. De Roubin, W. Satuła, and J. Suhonen, Phys. Rev. C **100**, 054333 (2019).

[50] F. G. Kondev, M. Wang, W. J. Huang, S. Naimi, and G. Audi, Chin. Phys. C **45**, 030001 (2021).

[51] K. Schmidt, C. Mazzocchi, R. Borcea, J. Döring, S. Galanopoulos, M. Gorska, H. Grawe, S. Harissopulos, M. Hellström, Z. Janas, R. Kirchner, G. Kriembardis, M. La Commara, A. N. Ostrowski, G. Rainovski, and E. Roeckl, Eur. Phys. J. A **8**, 303 (2000).

[52] N. Mărginean, C. Rusu, D. Bucurescu, C. R. Alvarez, C. A. Ur, D. Bazzacco, S. Lunardi, P. Pavan, G. de Angelis, M. Axiotis, E. Farnea, A. Gadea, M. Ionescu-Bujor, A. Iordachescu, W. Krolas, T. Kroll, S. M. Lenzi, T. Martinez, R. Menegazzo, D. R. Napoli, B. Quintana, P. Spolaore, Y. H. Zhang, and J. Wrzesinski, Phys. Rev. C **72**, 014302 (2005).

[53] C. V. Weiffenbach, S. Gujrathi, and J. K. P. Lee, Can. J. Phys. **53**, 101 (1975).

[54] D. Rudolph, C. J. Gross, A. Harder, M. K. Kabadiyski, K. P. Lieb, M. Weiszflog, J. Altmann, A. Dewald, J. Eberth, T. Mylaeus, H. Grawe, J. Heese, and K. H. Maier, Phys. Rev. C **49**, 66 (1994).

[55] J. Döring, H. Grawe, K. Schmidt, R. Borcea, S. Galanopoulos, M. Górska, S. Harissopulos, M. Hellström, Z. Janas, R. Kirchner, M. La Commara, C. Mazzocchi, E. Roeckl, and R. Schwengner, Phys. Rev. C **68**, 034306 (2003).

[56] I. Mardor, S. A. S. Andrés, T. Dickel, D. Amanbayev, S. Beck, J. Bergmann, H. Geissel, L. Gröf, E. Haettner, C. Hornung, N. Kalantar-Nayestanaki, G. Kripko-Koncz, I. Miskun, A. Mollaebrahimi, W. R. Plaß, C. Scheidenberger, H. Weick, S. Bagchi, D. L. Balabanski, A. A. Bezbakh *et al.*, Phys. Rev. C **103**, 034319 (2021).

[57] G. G. J. Boswell and T. McGee, J. Inorg. Nucl. Chem. **32**, 2805 (1970).

[58] J. A. Macdonald, J. C. Hardy, H. Schmeing, T. Faestermann, H. R. Andrews, J. S. Geiger, R. L. Graham, and K. P. Jackson, Nucl. Phys. A **288**, 1 (1977).

[59] A. Kankainen, L. Batist, S. A. Eliseev, V.-V. Elomaa, T. Eronen, U. Hager, J. Hakala, A. Jokinen, I. Moore, Y. N. Novikov, H. Penttilä, K. Peräjärvi, A. V. Popov, S. Rahaman, S. Rinta-Antila, P. Ronkanen, A. Saastamoinen, D. M. Seliverstov, T. Sonoda, G. K. Vorobjev, and J. Äystö, Eur. Phys. J. A **29**, 271 (2006).

[60] D. Rodríguez, G. Audi, J. Äystö, D. Beck, K. Blaum, G. Bollen, F. Herfurth, A. Jokinen, A. Kellerbauer, H.-J. Kluge, V. S. Kolhinen, M. Oinonen, E. Sauvan, and S. Schwarz, Nucl. Phys. A **769**, 1 (2006).

[61] T. Otto, G. Bollen, G. Savard, L. Schweikhard, H. Stolzenberg, G. Audi, R. B. Moore, G. Rouleau, J. Szerypo, Z. Patyk, and the ISOLDE Collaboration, Nucl. Phys. A **567**, 281 (1994).

[62] K. S. Sharma, E. Hagberg, G. R. Dyck, J. C. Hardy, V. T. Koslowsky, H. Schmeing, R. C. Barber, S. Yuan, W. Perry, and M. Watson, Phys. Rev. C **44**, 2439 (1991).

[63] B. E. Tomlin, C. J. Barton, N. V. Zamfir, M. A. Caprio, R. L. Gill, R. Krücken, J. R. Novak, J. R. Cooper, K. E. Zyromski, G. Cata-Danil, C. W. Beausang, A. Wolf, N. A. Pietralla, H. Newman, J. Cederkall, B. Liu, Z. Wang, R. F. Casten, and D. S. Brenner, Phys. Rev. C **63**, 034314 (2001).

[64] M. Hausmann, J. Stadlmann, F. Attallah, K. Beckert, P. Beller, F. Bosch, H. Eickhoff, M. Falch, B. Franczak, B. Franzke, H. Geissel, T. Kerscher, O. Klepper, H.-J. Kluge, C. Kozhuharov, Y. A. Litvinov, K. E. G. Löbner, G. Münzenberg, N. Nankov, F. Nolden *et al.*, Hyperfine Interact. **132**, 289 (2001).

[65] F. Herfurth, G. Audi, D. Beck, K. Blaum, G. Bollen, P. Delahaye, M. Dworschak, S. George, C. Guénaut, A. Kellerbauer, D. Lunney, M. Mukherjee, S. Rahaman, S. Schwarz, L. Schweikhard, C. Weber, and C. Yazidjian, Eur. Phys. J. A **47**, 75 (2011).

[66] I. Kulikov, A. Algora, D. Atanasov, P. Ascher, K. Blaum, R. B. Cakirli, A. Herlert, W. J. Huang, J. Karthein, Y. A. Litvinov, D. Lunney, V. Manea, M. Mougeot, L. Schweikhard, A. Welker, and F. Wienholtz, Nucl. Phys. A **1002**, 121990 (2020).

[67] National Nuclear Data Center, https://www.nndc.bnl.gov.

[68] Yu. A. Litvinov, F. Attallah, K. Beckert, F. Bosch, D. Boutin, M. Falch, B. Franzke, H. Geissel, M. Hausmann, Th. Kerscher, O. Klepper, H.-J. Kluge, C. Kozhuharov, K. E. G. Löbner, G. Münzenberg, F. Nolden, Yu. N. Novikov, Z. Patyk, T. Radon, C. Scheidenberger, J. Stadlmann *et al.*, Phys. Lett. B **573**, 80 (2003).

[69] M. W. Reed, I. J. Cullen, P. M. Walker, Yu. A. Litvinov, K. Blaum, F. Bosch, C. Brandau, J. J. Carroll, D. M. Cullen, A. Y. Deo, B. Detwiller, C. Dimopoulou, G. D. Dracoulis, F. Farinon, H. Geissel, E. Haettner, M. Heil, R. S. Kempley, R. Knöbel, C. Kozhuharov *et al.*, Phys. Rev. Lett. **105**, 172501 (2010).

[70] J. Heese, N. Martin, C. J. Gross, W. Fieber, K. P. Lieb, A. Kuhnert, K. H. Maier, and X. Sun, Phys. Rev. C **41**, 1553 (1990).

[71] C. Miehé, P. Dessagne, C. Pujol, G. Walter, B. Jonson, M. Lindroos, and the ISOLDE Collaboration, Eur. Phys. J. A **5**, 143 (1999).

[72] O. Kavatsyuk, M. Kavatsyuk, L. Batist, A. Banu, F. Becker, A. Blazhev, W. Brüchle, J. Döring, T. Faestermann, M. Górska, H. Grawe, Z. Janas, A. Jungclaus, M. Karny, R. Kirchner, M. La Commara, S. Mandal, C. Mazzocchi, I. Mukha, S. Muralithar, C. Plettner *et al.*, Eur. Phys. J. A **25**, 211 (2005).

[73] W. J. Huang, G. Audi, M. Wang, F. G. Kondev, S. Naimi, and X. Xu, Chin. Phys. C **41**, 030002 (2017); M. Wang, G. Audi, F. G. Kondev, W. J. Huang, S. Naimi, and X. Xu, *ibid.* **41**, 030003 (2017).

[74] K. Auranen, D. Seweryniak, M. Albers, A. D. Ayangeakaa, S. Bottoni, M. P. Carpenter, C. J. Chiara, P. Copp, H. M. David, D. T. Doherty, J. Harker, C. R. Hoffman, R. V. F. Janssens, T. L. Khoo, S. A. Kuvin, T. Lauritsen, G. Lotay, A. M. Rogers, C. Scholey, J. Sethi *et al.*, Phys. Lett. B **792**, 187 (2019).

[75] R. D. Page, P. J. Woods, R. A. Cunningham, T. Davinson, N. J. Davis, A. N. James, K. Livingston, P. J. Sellin, and A. C. Shotter, Phys. Rev. Lett. **72**, 1798 (1994).
[76] D. Schardt, R. Kirchner, O. Klepper, W. Reisdorf, E. Roeckl, P. Tidemandpetersson, G. T. Ewan, E. Hagberg, B. Jonson, S. Mattsson, and G. Nyman, Nucl. Phys. A **326**, 65 (1979).
[77] F. Heine, T. Faestermann, A. Gillitzer, J. Homolka, M. Köpf, and W. Wagner, Z. Phys. A **340**, 225 (1991).
[78] J. Fallis, J. A. Clark, K. S. Sharma, G. Savard, F. Buchinger, S. Caldwell, J. E. Crawford, C. M. Deibel, J. L. Fisker, S. Gulick, A. A. Hecht, D. Lascar, J. K. P. Lee, A. F. Levand, G. Li, B. F. Lundgren, A. Parikh, S. Russell, M. S. V. de Vorst, N. D. Scielzo *et al.*, Phys. Rev. C **78**, 022801(R) (2008).
[79] E. Hagberg, J. C. Hardy, H. Schmeing, E. T. H. Clifford, and V. T. Koslowsky, Nucl. Phys. A **395**, 152 (1983).
[80] X. L. Tu, A. Kelić-Heil, Y. A. Litvinov, Z. Podolyàk, Y. H. Zhang, W. J. Huang, H. S. Xu, K. Blaum, F. Bosch, R. J. Chen, X. C. Chen, C. Y. Fu, B. S. Gao, Z. Ge, Z. G. Hu, D. W. Liu, S. A. Litvinov, X. W. Ma, R. S. Mao, B. Mei *et al.*, Phys. Rev. C **95**, 014610 (2017).
[81] T. Otsuka, A. Gade, O. Sorlin, T. Suzuki, and Y. Utsuno, Rev. Mod. Phys. **92**, 015002 (2020).
[82] T. Otsuka, Phys. Scr. T **152**, 014007 (2013).
[83] D. Steppenbeck, S. Takeuchi, N. Aoi, P. Doornenbal, M. Matsushita, H. Wang, H. Baba, N. Fukuda, S. Go, M. Honma, J. Lee, K. Matsui, S. Michimasa, T. Motobayashi, D. Nishimura, T. Otsuka, H. Sakurai, Y. Shiga, P.-A. Söderström, T. Sumikama *et al.*, Nature (London) **502**, 207 (2013).
[84] N. Shimizu, T. Mizusaki, Y. Utsuno, and Y. Tsunoda, Comput. Phys. Commun. **244**, 372 (2019).
[85] G. Bertsch, J. Borysowicz, H. Mcmanus, and W. G. Love, Nucl. Phys. A **284**, 399 (1977).
[86] T. Otsuka, T. Suzuki, M. Honma, Y. Utsuno, N. Tsunoda, K. Tsukiyama, and M. Hjorth-Jensen, Phys. Rev. Lett. **104**, 012501 (2010).
[87] T. Togashi, N. Shimizu, Y. Utsuno, T. Otsuka, and M. Honma, Phys. Rev. C **91**, 024320 (2015).
[88] C. Yuan, Z. Liu, F. R. Xu, P. M. Walker, Z. Podolyák, C. Xu, Z. Z. Ren, B. Ding, M. L. Liu, X. Y. Liu, H. S. Xu, Y. H. Zhang, X. H. Zhou, and W. Zuo, Phys. Lett. B **762**, 237 (2016).
[89] M. Queiser, A. Vogt, M. Seidlitz, P. Reiter, T. Togashi, N. Shimizu, Y. Utsuno, T. Otsuka, M. Honma, P. Petkov, K. Arnswald, R. Altenkirch, B. Birkenbach, A. Blazhev, T. Braunroth, A. Dewald, J. Eberth, C. Fransen, B. Fu, H. Hess *et al.*, Phys. Rev. C **96**, 044313 (2017).
[90] M. Wang, M. Zhang, X. Zhou, Y. H. Zhang, Y. A. Litvinov, H. S. Xu, R. J. Chen, H. Y. Deng, C. Y. Fu, W. W. Ge, H. F. Li, T. Liao, S. A. Litvinov, P. Shuai, J. Y. Shi, M. Si, R. S. Sidhu, Y. N. Song, M. Z. Sun, S. Suzuki *et al.*, Phys. Rev. C **106**, L051301 (2022).
[91] X. Zhou, M. Zhang, M. Wang, Y. H. Zhang, Y. J. Yuan, X. L. Yan, X. H. Zhou, H. S. Xu, X. C. Chen, Y. M. Xing, R. J. Chen, X. Xu, P. Shuai, C. Y. Fu, Q. Zeng, M. Z. Sun, H. F. Li, Q. Wang, T. Bao, M. Si *et al.*, Phys. Rev. Accel. Beams **24**, 042802 (2021).